

This is the **submitted version** of the journal article:

Yu, Xuelian; An, Xiaoqiang; Genç, Aziz; [et al.]. «Cu₂ZnSnS₄-PtM (M = Co, Ni) nanoheterostructures for photocatalytic hydrogen evolution». Journal of physical chemistry. C, Vol. 119, issue 38 (Sep. 2015), p. 21882-21888. DOI 10.1021/acs.jpcc.5b06199

This version is available at <https://ddd.uab.cat/record/270836>

under the terms of the  **CC BY-NC-ND** license

Cu₂ZnSnS₄-PtM (M = Co, Ni) Nano-Heterostructures for Photocatalytic Hydrogen Evolution

Xuelian Yu,^[a,b] Xiaoqiang An,^[c] Aziz Genç,^[d] Maria Ibáñez,^[b] Jordi Arbiol,^[d,e] Yihe Zhang,^{[a]} and
Andreu Cabot^{*[b,e]}*

[a] Beijing Key Laboratory of Materials Utilization of Nonmetallic Minerals and Solid Wastes, National Laboratory of Mineral Materials, School of Materials Science and Technology, China University of Geosciences, 100083, Beijing, P. R. China

[b] Catalonia Energy Research Institute - IREC, 08930, Sant Adria del Besos, Barcelona, Spain

[c] Key Laboratory of Drinking Water Science and Technology, Research Center for Eco-Environmental Sciences, Chinese Academy of Sciences, 100085, Beijing, P. R. China

[d] Institut Català de Nanociència i Nanotecnologia, ICN2, Campus de la UAB, 08193 Bellaterra, Spain

[e] Institució Catalana de Recerca i Estudis Avançats - ICREA, 08010, Barcelona, Spain

Cu₂ZnSnS₄-PtM (M = Co, Ni) Nano-Heterostructures for Photocatalytic Hydrogen Evolution

ABSTRACT We report the synthesis and photocatalytic and magnetic characterization of colloidal nano-heterostructures formed by combining a Pt-based magnetic metal alloy (PtCo, PtNi) with Cu₂ZnSnS₄ (CZTS). While CZTS is one of the main candidate materials for solar energy conversion, the introduction of a Pt-based alloy on its surface strongly influences its chemical and electronic properties, ultimately determining its functionality. In this regard, up to a 15-fold increase of the photocatalytic hydrogen evolution activity was obtained with CZTS-PtCo when compared with CZTS. Furthermore, twice higher hydrogen evolution rates were obtained for CZTS-PtCo when compared with CZTS-Pt, in spite of the lower precious metal loading of the former. Besides, the magnetic properties of the PtCo nanoparticles attached to the CZTS nanocrystals were retained in the heterostructures, what could facilitate catalyst purification and recovery for its posterior recycling and/or reutilization.

Introduction

Maximizing material performance in a particular application frequently requires the simultaneous optimization of several functional properties. In the field of photocatalysis, the material needs to be able to absorb the major part of the solar spectra, to adsorb the reactants and generally to efficiently exchange charge with them. In quasi-homogeneous photocatalytic systems involving colloidal nanoparticles, it is also necessary to ensure the suspension stability and to introduce a mechanism for material recovery. Such multifunctionality is generally incompatible with the limited parameters of a single material, thus the engineering of heterostructures and particularly nano-heterostructures has a remarkable fundamental and technological interest.

$\text{Cu}_2\text{ZnSnS}_4$ (CZTS) has been recently proposed as an alternative absorber to more conventional CdTe and $\text{Cu}(\text{In,Ga})\text{Se}_2$ semiconductors. Compared with these binary and ternary/quaternary compounds, CZTS is made of more abundant and lower toxicity elements, while conserving an optimal direct band gap of 1.5 eV and a large absorption coefficient.¹¹ CZTS has been shown as an excellent light absorber not only for solar energy conversion through photovoltaics, but also for photocatalytic generation of hydrogen and other value-added chemicals and for photodegradation of pollutants.^{12,13}

On the other hand, platinum is the most used catalyst for hydrogen evolution due to its excellent catalytic activity.⁴ However, Pt is a rare and thus expensive element, whose usage needs to be minimized in practical applications. One way to reduce the amount of Pt used is by increasing its activity and maximizing the ratio of atoms exposed to the media.^{5, Chem. Commun., 2011, 47, 3885-3887} A second strategy to minimize the amount of Pt, is to alloy it with lower cost transition metals.^{6, Chem. Rev., 2012, 112}

(11), pp 5780–5817 In this direction, bimetallic catalysts not only have made possible to reduce the amount

of expensive noble metals used, but they have further allowed to modify the electronic and chemical properties of the noble metal, enabling the engineering of catalysts with improved activities, selectivities and stabilities. ^{Chem. Rev., 2012, 112 (11), pp 5780–5817} In particular, bimetallic Pt-Co and Pt-Ni alloys are well-known oxygen reduction electrocatalysts. ^{J. Phys. Chem. B, 2002, 106 (16), pp 4181–4191, Journal of Power Sources, Volume 160, Issue 2, 6 October 2006, Pages 957–968, J. Electrochem. Soc. 1990 volume 137, issue 11, 3368-3374, *J. Phys. Chem. B*, 2002, 106 (8), pp 1869–1877, *J. Phys. Chem. B*, 2004, 108 (30), pp 11024–11034, FUEL CELLS 2001, 1, No. 2 105-116} They have been also proposed for hydrogenation reactions, ^{Journal of Catalysis Volume 156, Issue 1, September 1995, Pages 85–95; Fuel Volume 132, 15 September 2014, Pages 62–70, J. Am. Chem. Soc., 2012, 134 (21), pp 8975–8981} hydrogen generation, ^{9, Chem. Soc. Rev., 2012, 41, 7994-8008} and recently even as counter electrode in dye-sensitized solar cells when supported on $\text{Cu}_2\text{ZnGeS}_4$.⁸

Herein, monodisperse CZTS nanocrystals were synthesized and used as support to produce CZTS-PtCo and CZTS-PtNi nano-heterostructures. CZTS-PtCo metal-semiconductor nano-heterostructures were characterized by higher photocatalytic activities toward hydrogen generation from water when compared not only with the bare CZTS semiconductor, but also with CZTS-Pt. They also show a potentially convenient magnetic moment.

Experimental

Chemicals and solvents: Tert-dodecylmercaptan, dodecanethiol, tin(IV) chloride ($\text{SnCl}_4 \cdot 5\text{H}_2\text{O}$), zinc oxide (ZnO), copper(II) chloride ($\text{CuCl}_2 \cdot 2\text{H}_2\text{O}$), platinum(II) acetylacetonate, nickel(II) acetate, cobalt(II) acetate, 1-octadene (ODE), oleylamine (OLA, 70%), oleic acid (OA, 90 %) were purchased from Aldrich. Chloroform, isopropanol, tetrahydrofuran, toluene and methanol were of analytical grade and obtained from various sources.

Synthesis of CZTS-metal alloy heterostructures: Quasi-spherical CZTS nanoparticles with wurtzite structure were prepared by the reaction of copper, tin and zinc salts with a mixture of the tert-dodecylmercaptan and dodecanethiol in the presence of oleylamine (OLA) as we previously described.¹³ CZTS-Pt, CZTS-PtCo and CZTS-PtNi nano-heterostructures were prepared from the nucleation of Pt, PtCo or PtNi on the surface of the quasi-spherical CZTS nanoparticles. In a typical synthesis, oleic acid (0.20 mL), oleylamine (0.20 mL), 1,2-hexadecanediol (43 mg), and phenyl ether (10 mL) were loaded into a reaction flask and kept **under vacuum?** at 120 °C for 30 min. Then, the mixture was purged with nitrogen and heated to 200 °C. In another flask, CZTS nanocrystals (**how many mg?**) were mixed with platinum(II) acetylacetonate (40 mg) and different amounts of cobalt acetate or nickel acetate and the mixture was heated at 80 °C for 10 min **under vacuum?**. Then, the metal precursor solution containing the CZTS nanoparticles was injected into the surfactant solution maintained at 200 °C. After 10 min, the reaction was quenched in a water bath. The final product was washed by multiple precipitation/dispersion cycles with toluene and ethanol, and it was finally dispersed in toluene.

Characterization techniques: The morphological, chemical and structural characterizations of the nanoparticles were carried out by transmission electron microscopy (TEM) and high-resolution TEM (HRTEM). Carbon-coated TEM grids from Ted-Pella were used as substrates. HRTEM images were obtained using a FEI Tecnai F20 field-emission gun microscope with a 0.19 nm point- to-point resolution at 200 keV with an embedded Gatan image filter for EELS analyses. Images were analyzed by means of Gatan Digital micrograph software.

Scanning electron microscopy (SEM) was performed using a ZEISS Auriga SEM with an energy dispersive X-ray spectroscopy (EDS) detector to study composition. Powder X-ray diffraction (XRD) patterns were obtained with Cu K α 1 ($\lambda = 1.5406 \text{ \AA}$) radiation in a reflection geometry on a Bruker D8

operating at 40 kV and 40 mA. Ultraviolet-visible-near infrared spectroscopy (UV-Vis-NIR) spectra were recorded on a LAMBDA 950 UV-Vis spectrophotometer from PerkinElmer. X-ray photoelectron spectroscopic (XPS) measurements were performed on a Thermo Scientific XPS spectrometer. Field-dependent magnetization measurements (M-H) were conducted with a SQUID magnetometer (Quantum Design MPMS XL) at 5K.

Photocatalytic hydrogen generation experiments

Nanocrystals were rendered water soluble by replacing the initial surfactants with $[\text{NH}_4]_2\text{S}$. For the photocatalytic H_2 generation experiments, 10 mg of nanoparticles was dispersed in 50 ml of deionized water, containing 0.1 M Na_2S and Na_2SO_3 as hole scavengers. Before irradiating the solution, the reactor was thoroughly purged with argon to remove all oxygen in the headspace of the reactor and dissolved in water. A baseline was taken to ensure that there was no detectable oxygen in the system. A 300 W Xe lamp (Newport) was used to irradiate the sample after a suitable baseline was obtained. The reaction product was monitored by periodically sampling the gas phase from the glass chamber using a gas tight syringe and analyzing it by a gas chromatograph (Varian GC-450). Argon was used as the gas chromatograph (GC) carrier gas.

Fabrication of thin film electrodes and electrochemical measurements

5 mg of photocatalysts and 10 μL of Nafion solution (5 wt%) were dispersed using sonication in 1 mL water/isopropanol mixed solvent (3:1 v/v) until forming a homogeneous catalyst ink. 100 μL of this ink was deposited onto 1 cm^2 FTO-coated glass to fabricate the working electrode. A platinum wire was used as a counter electrode, and an Ag/AgCl reference electrode completed the three-electrode electrochemical system. Electrochemical impedance spectrometry (EIS) experiments in the frequency range 0.1 Hz - 100 KHz were carried out on a Zahner Zennium electrochemical workstation (Zahner

Instrument Inc., Germany) in the presence of a 1 mM $\text{K}_3[\text{Fe}(\text{CN})_6]/\text{K}_4[\text{Fe}(\text{CN})_6]$ (1:1) mixture as a redox probe in 0.1 M KCl aqueous solution. The signal amplitude was set to 5 mV.

Results and discussion

Representative TEM micrographs of the CZTS nanoparticles used to support the bimetallic nanocrystals are shown in Figure 1a. CZTS nanoparticles were characterized by a quasi-spherical morphology and an average size of 12 nm. XRD analysis (Figure S11) showed their crystal structure to be that of wurtzite. This crystal phase was confirmed by HRTEM analysis (Figure 2)

CZTS-PtCo nano-heterostructures obtained with different nominal Co/Pt ratios (0, 0.5, 1, 2) were produced as detailed in the experimental sections. After metal deposition, no significant change in the size and shape of the CZTS nanocrystals was observed by TEM analysis. However, TEM micrographs clearly displayed small higher-contrast spots homogeneously distributed over the CZTS nanocrystal surface (Figure 1b-1d). This higher contrast spots had average sizes in between 1 and 2 nm for the CZTS-PtCo nano-heterostructures with the lowest nominal Co/Pt molar ratios tested (Co/Pt = 0.5) and of around 3 nm for the highest (Co/Pt = 2). EDS analysis revealed that both Pt and Co were present on the final material (Figure S12). The metal ratios increased with the increase of the ratio of cobalt and platinum acetates introduced in the precursor mixture, although slight deviations from the nominal values were obtained (Table S11).¹⁴

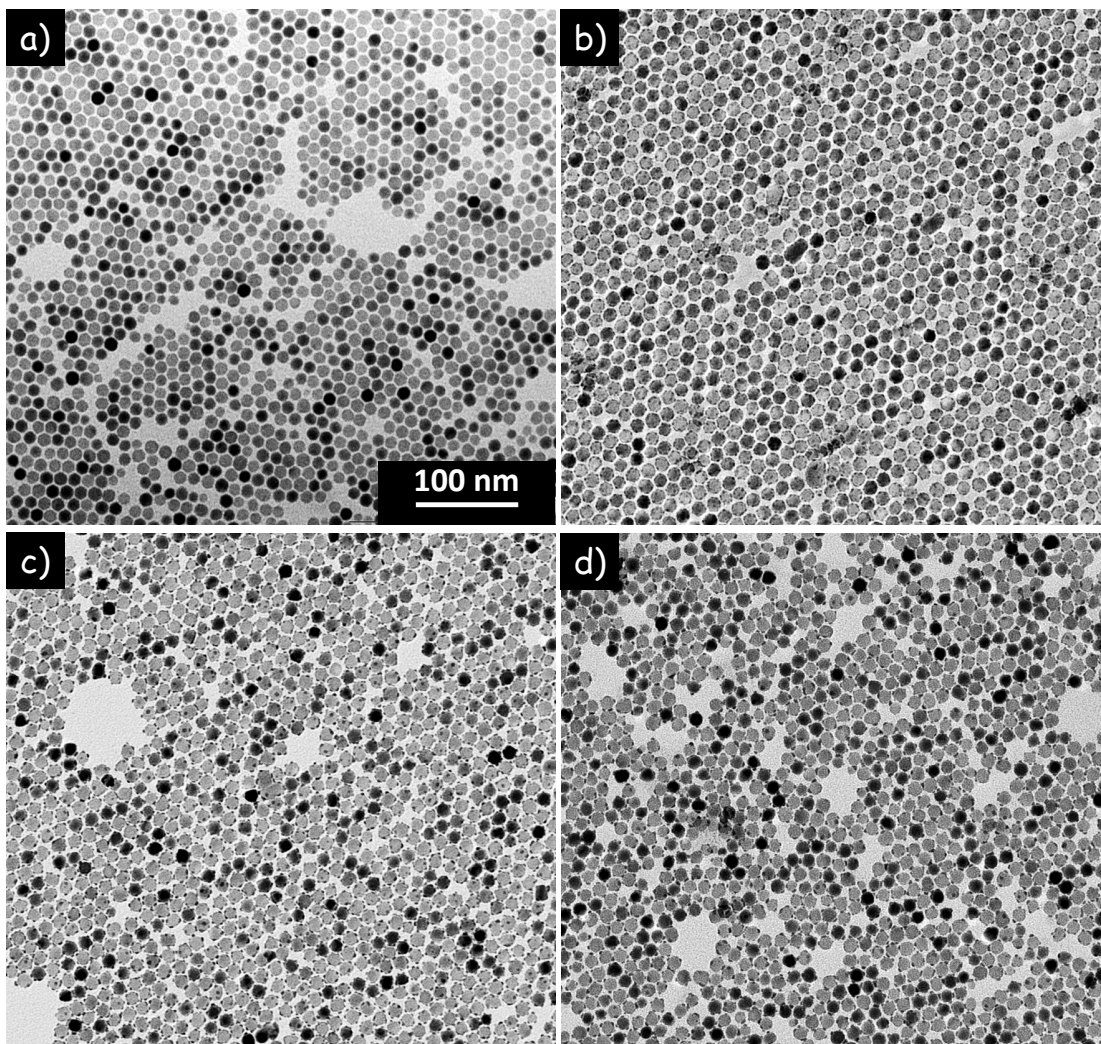


Figure 1. Representative TEM images of CZTS nanoparticles (a) and CZTS-PtCo nano-heterostructures with different nominal Co/Pt ratios: Co/Pt = 0.5 (b); Co/Pt = 1 (c); Co/Pt = 2 (d).

Figures 2a and 2b show higher magnification TEM and STEM-HAADF micrographs of the CZTS-PtCo (Co/Pt=0.5) sample. STEM-HAADF micrograph shows the CZTS surfaces to be randomly decorated with multiple 1-2 nm metal (brighter contrast) nanocrystals. Figure 2c and 2d show two HRTEM micrographs obtained with certain defocus in order to reveal the presence of the metal nanocrystals. When the CZTS nanoparticle is in perfect focus, just the CZTS nanoparticles were seen. Only when imaging the nanoparticles in under-focus conditions, the black dots associated to PtCo

started to appear around the nanoparticles. This experimental evidence indicated that no epitaxial relation existed between the metal and the semiconductor nanocrystals. Figure 2h displays a 3D structural model of a faceted CZTS nanoparticle decorated with several ~ 2 nm f.c.c. PtCo NPs. S. Bernal, F.J. Botana, J.J. Calvino, C. López-Cartes, J.A. Pérez-Omil, J.M. Rodríguez-Izquierdo, The interpretation of HREM images of supported metal catalysts using image simulation: Profile view images, *Ultramicroscopy*, 72 (1998) 135-164.

CZTS-PtCo nano-heterostructures obtained with higher Co/Pt ratios displayed slightly larger PtCo nanocrystals (Figure 2e). HRTEM characterization of CZTS-PtCo (Co/Pt = 2) showed the metal nanocrystals to be crystalline and tightly anchored to CZTS, although no epitaxial relation could be identified (Figure 2f). In figure 2g a HRTEM micrograph of a single CZTS nano-heterostructure is displayed. The lower contrast lattice of the support nanoparticle has an interplanar distance of 0.32 nm, which corresponds to the (002) plane of CZTS. The interplanar distance of the higher contrast nanocrystal was 0.22, which is slightly smaller to the (111) interplanar distance of Pt (0.23 nm). This slight difference is most probably related to a decrease of the lattice parameter when replacing part of the Pt by Co to form the PtCo alloy.

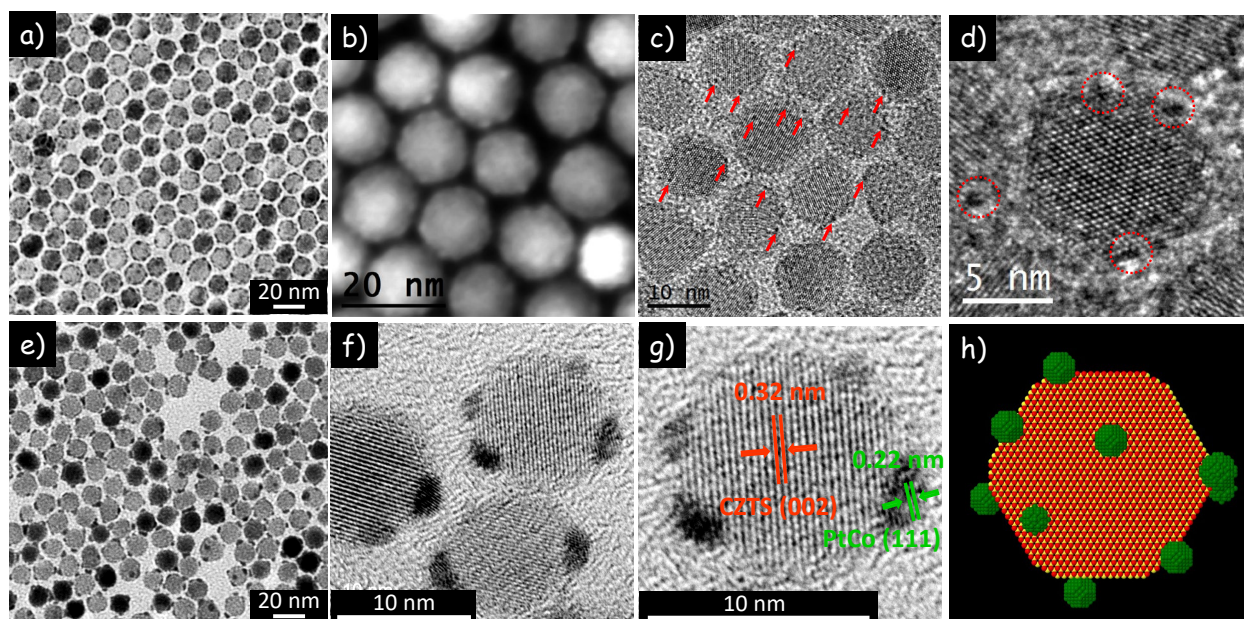


Figure 2. Top row: TEM (a), STEM-HAADF (b) and HRTEM (c,d) micrographs of CZTS-PtCo nano-heterostructures with $[Co]/[Pt]=0.5$. Micrographs show the ~ 12 nm faceted CZTS nanoparticles decorated with $\sim 1-2$ nm PtCo nanocrystals as pointed with arrows in (c) and circled in (d). Bottom row: TEM (e) and HRTEM (f,g) micrograph of CZTS-PtCo nano-heterostructures with $[Co]/[Pt]=2$. Micrographs show the ~ 12 nm faceted CZTS nanoparticles decorated with ~ 3 nm PtCo nanocrystals. A structural model of a faceted wurtzite CZTS nanocrystal randomly decorated with ~ 2 nm f.c.c. PtCo NPs is shown in (h). Color code: Cu, Zn and Sn atoms in red; S atoms in yellow; and Pt and Co in green.

Figure 3 shows the Pt 4f and Co 2p XPS spectra obtained from CZTS-Pt and CZTS-PtCo nano-heterostructures. As for monometallic CZTS-Pt (Figure 3a),¹⁵ the Pt 4f spectrum of CZTS-PtCo (Figure 3b) presented relatively broad bands, which pointed out to the presence of at least two pairs of doublets and thus two Pt chemically states, Pt^0 and Pt^{2+} . From the fitting of the spectra it became clear that in both samples the metallic Pt^0 state is the main component. It is also evident that the Pt^0 peak in the CZTS-PtCo samples is slightly shifted to higher binding energies than that of CZTS-Pt (Figure 3c). This positive shift is attributed to a slight Pt electron loss and is a hallmark of the Pt-Co alloying.¹⁶ Similarly, two pairs of doublets were also fitted to the Co 2p binding energy region (Figure 3d), being the stronger peaks associated with Co^0 and the weaker to Co^{2+} . The presence of Co^{2+} in PtCo alloys is a common observation due to the easy oxidization of Co when exposed to air.¹⁷⁻¹⁸

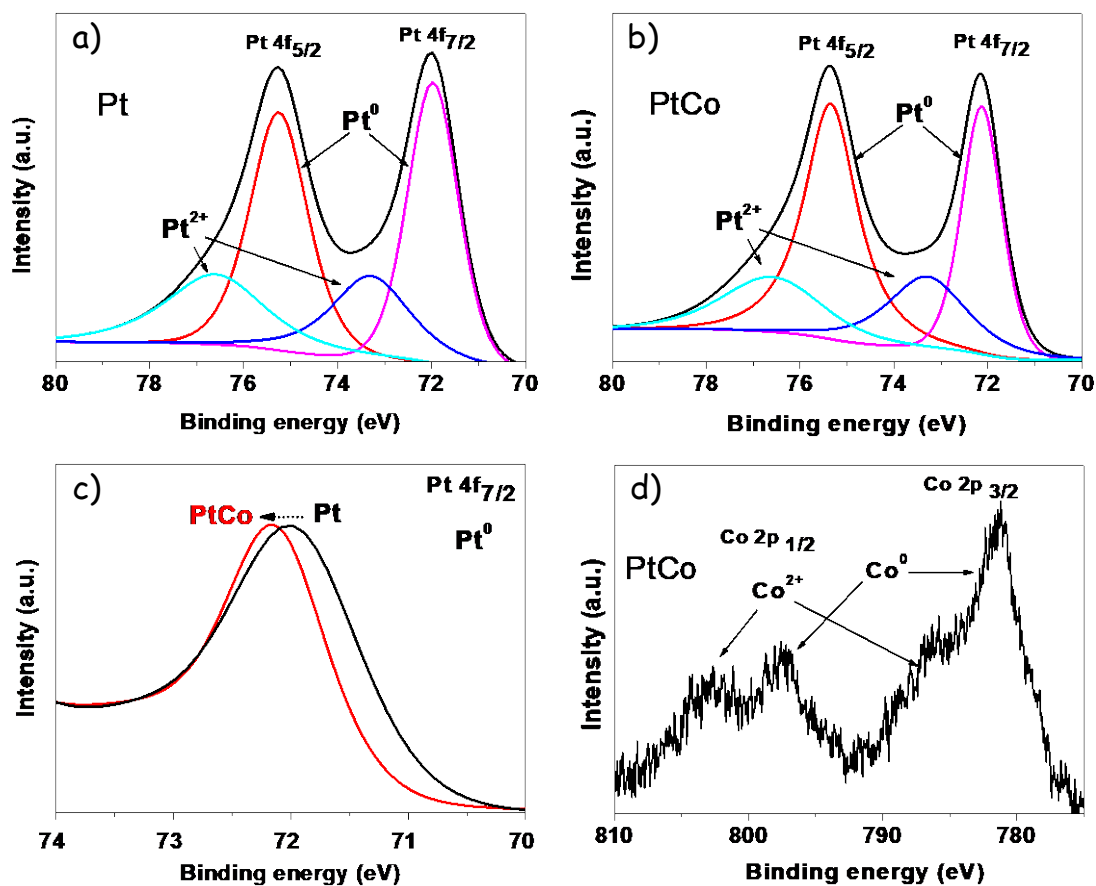


Figure 3. (a) XPS Pt 4f spectra for CZTS-Pt. (b) XPS Pt 4f spectra for CZTS-PtCo (Co/Pt=1). (c) Comparison of the fitted Pt⁰ sub-spectra of Pt 4f_{7/2} for CZTS-Pt and CZTS-PtCo. (d) XPS Co 2p spectra for CZTS-PtCo (Co/Pt=1).

CZTS-PtNi (Ni/Pt=1) nano-heterostructures were prepared following the same synthesis procedure. As described for PtCo, multiple PtNi nanoparticles with an average size of ~2 nm were randomly grown on the surface of the CZTS nanocrystals by adding nickel acetate to the growth solution (Figure 4a). EDS (Figure SI3), XPS (Figure SI4) and ICP (Table SI2) analysis showed the presence of both Pt and Ni with a ratio Ni/Pt = 0.64. The XPS binding energies of the Ni 2p_{3/2} and 2p_{1/2} states were located at 856.0 and 873.4 eV, respectively, which agreed with the literature values for metallic Ni⁰.¹⁹

Figure 4b displays a STEM-HAADF micrograph of the CZTS-PtNi nano-heterostructures showing several CZTS nanoparticles decorated by numerous PtNi nanocrystals in brighter contrast. An EDX line scan was obtained through the arrow displayed in the STEM-HAADF micrograph. While the intensity scale between the elemental counts and STEM intensity are not proportional, it is clear that the brighter metal spots are composed by both Pt and Ni.

Figure 4c shows a HRTEM micrograph of a CZTS-PtNi nano-heterostructure where the CZTS nanoparticle and two attached $\sim 2\text{-}3$ nm PtNi nanoparticles are in fairly good zone axes and clearly visible. In the middle, FFTs from the CZTS and upper PtNi are shown. A power spectrum (FFT) obtained from the CZTS nanoparticle reveals its wurtzite phase with lattice parameters of $a = b = 0.3839$ nm and $c = 0.6339$ nm (space group = $P6_3mc$) and visualized along $[10\text{-}31]$ zone axis. The power spectrum of the green squared region reveals that the surface nanocrystal comprises a face centered cubic PtNi phase (space group = $Fm\bar{3}m$) with a lattice parameter of $a = 0.387$ nm and visualized along its $[011]$ zone axis. On the right (Figure 4d), a color structural map showing the wurtzite CZTS phase in red and f.c.c PtNi phase in green is shown, where it is clear that there is an epitaxy between the base CZTS and attached PtNi nanoparticles. In the lower row, several epitaxial relations between the CZTS and PtNi nanoparticles from the areas indicated with red and green squares are shown. First serie on the right shows the epitaxial relation between $\{1\text{-}10\text{-}1\}$ or $\{01\text{-}1\text{-}1\}$ planes of CZTS (blue circles) and $\{111\}$ planes of PtNi (yellow circles), where there are 5 PtNi planes for every 4 CZTS planes (indicated with black parentheses) with a total lattice mismatch of $\sim 7\%$. The same epitaxial relation is observed between the CZTS and the lower PtNi nanocrystal (shown on the far right). Another possible epitaxy is shown (in the middle) between the $\{10\text{-}1\text{-}2\}$ planes of CZTS and $\{200\}$ planes of PtNi where there is 1 PtNi plane for every 1 CZTS planes but the lattice mismatch for this epitaxial relation is quite high ($\sim 17\%$).

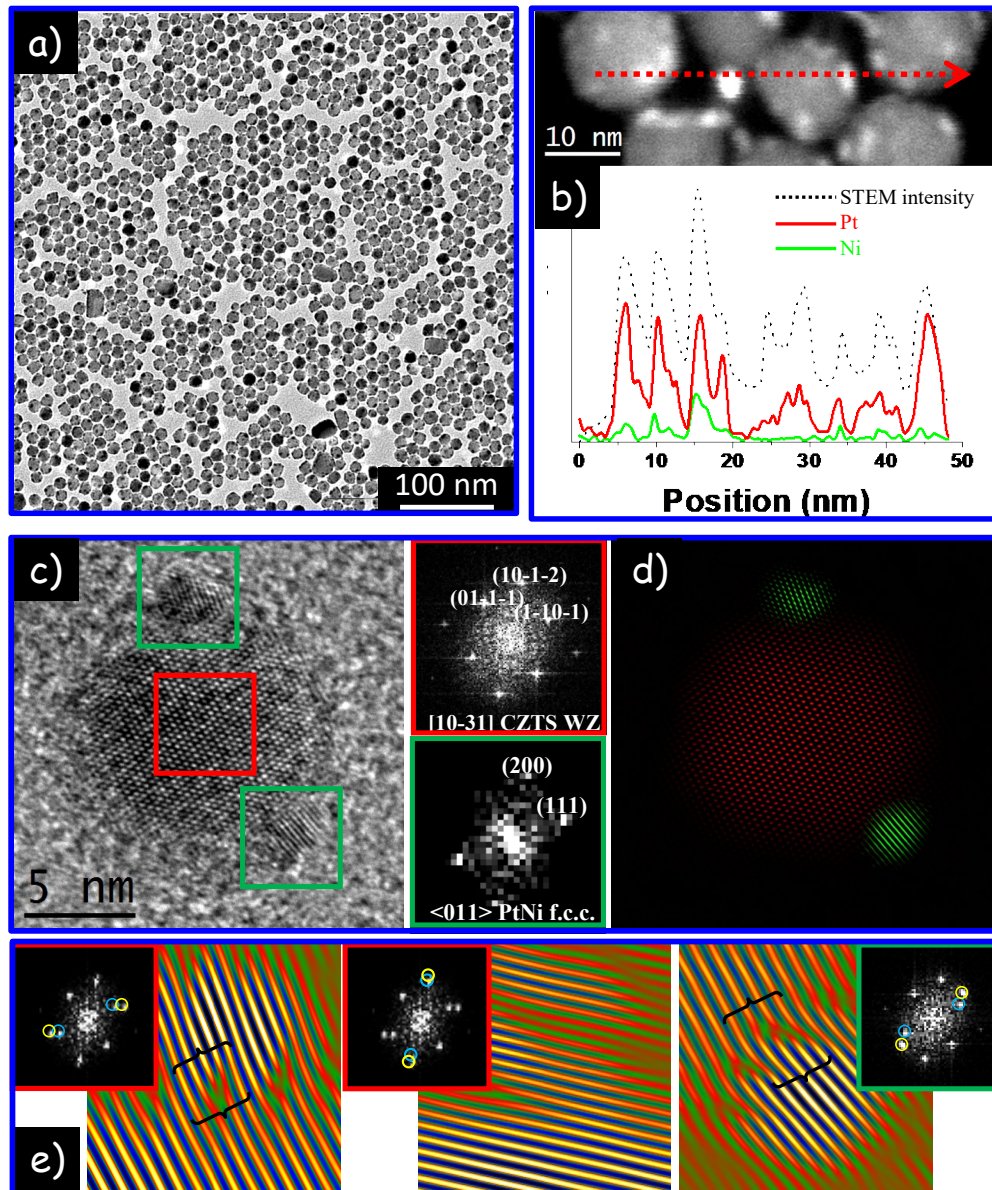


Figure 4. a) TEM micrograph of CZTS-PtNi nano-heterostructures. b) STEM-HAADF micrographs showing PtNi nanoparticles in brighter contrast and EDX line scan through the arrow in the STEM-HAADF micrograph. Intensity scale between the elemental counts and STEM intensity are not proportional. c) HRTEM micrograph showing two PtNi nanoparticles attached to a CZTS nanoparticle and power spectra obtained from the CZTS and the upper PtNi nanoparticle. d) Color structural map of the CZTS (in red) and PtNi (in green). e) Different epitaxial relations between the CZTS and PtNi nanoparticles.

To illustrate the influence of inexpensive Co alloying on the CZTS photocatalytic properties, CZTS-PtCo nano-heterostructures were transferred from toluene to water by means of a ligand exchange with $(\text{NH}_4)_2\text{S}$. Figure 5a shows the activities of CZTS, CZTS-Pt and CZTS-PtCo metal alloy heterostructures with different nominal Co/Pt ratios. The photocatalytic H_2 evolution activity of CZTS ($0.13\text{mmol/g}\cdot\text{h}$) was relatively low due to a rapid recombination of photogenerated charge carriers. The activity was greatly enhanced to $1.02\text{mmol/g}\cdot\text{h}$ in the presence of Pt, as Pt reduces the overpotential in the production of H_2 from water.²⁰ CZTS-PtCo nano-heterostructures, with H_2 evolution rates up to $1.85\text{mmol/g}\cdot\text{h}$, were even more active than CZTS-Pt. H_2 evolution rates up to 15-fold higher than pure CZTS nanocrystals and almost 2-fold higher than CZTS-Pt were measured. The superior performance of CZTS-PtCo indicated these heterostructures could not only reduce the high price of noble metals, but also enhance their catalytic activity. Highest H_2 production rates were obtained for a nominal molar ratio $\text{Co/Pt}=1$. Further increasing the amount of Co caused a drop in the activity to $0.74\text{mmol/g}\cdot\text{h}$. The decrease of photocatalytic activity with the higher Co content might be induced by the increase of the nanocrystal size, thus reducing the total metal surface area, but also by a reduced number of active Pt site on the particle surface, which would decrease adsorption of hydrogen ions that preferentially take place on Pt instead of Co.

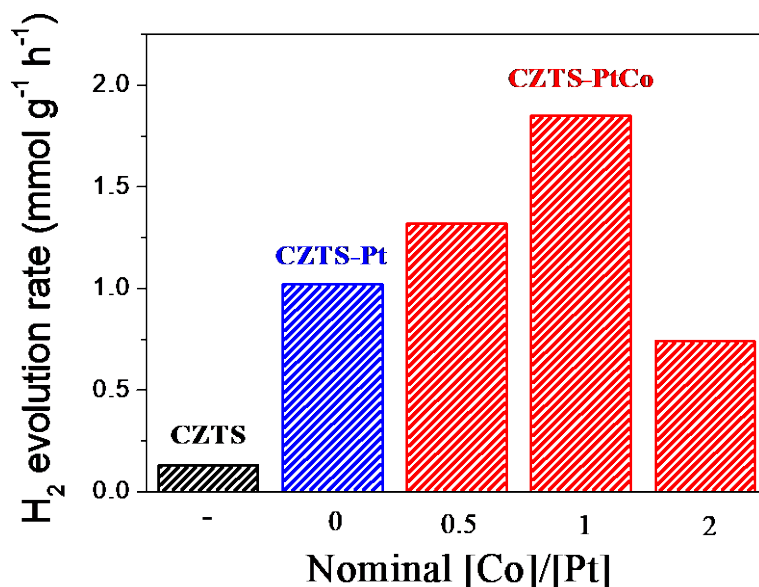


Figure 5. Comparison of photocatalytic H₂ evolution activity of CZTS, CZTS-Pt, CZTS-Pt₂Co, CZTS-PtCo and CZTS-PtCo₂ under full-arc light irradiation.

Main key parameters determining the photocatalytic hydrogen production rate are charge carriers photogeneration, separation and transport efficiencies.²¹ As no significant difference in the absorption spectra of CZTS nanocrystals was obtained when introducing Pt and PtCo (Figure SI5), we assume that the presence of neither the noble metal or the metal alloy increased the charge carrier photogeneration. To better understand the role of cobalt in the photocatalytic H₂ generation, the carrier dynamics in the photocatalysts were analyzed by electrochemical impedance spectra (EIS). As shown in Figure 6, the radius of the semicircle in the Nyquist plots, which is proportional to charge transfer resistance, of CZTS was much larger than that of CZTS-Pt and CZTS-PtCo nanocrystals. These differences indicated that the transport of charge carriers was indeed significantly influenced by the formation of the semiconductor-metal nano-heterostructures. Furthermore, the radius of the semicircle obtained with the CZTS-PtCo electrode was even smaller than that of CZTS-Pt, indicating a lower interface and thus charge transfer resistance from the material surface to the solution.²²

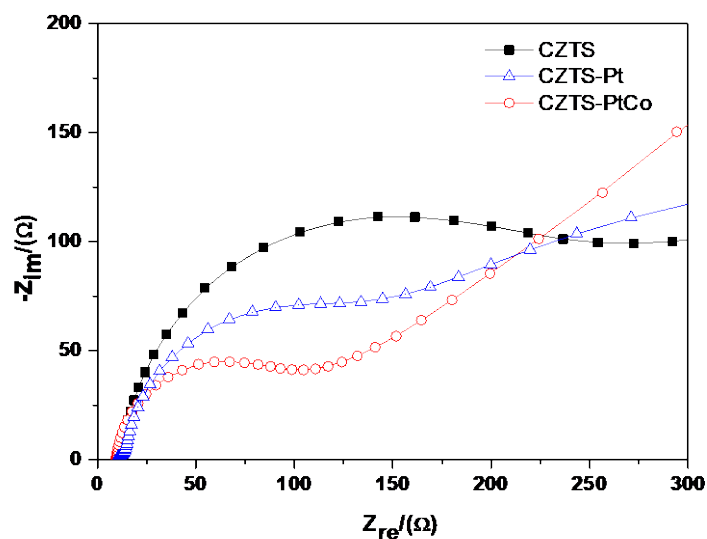


Figure 6. Electrochemical impedance spectra of CZTS, CZTS-Pt and CZTS-PtCo (Co/Pt=1) nanocrystals modified electrodes.

Besides, alloying Pt with Co may facilitate the accumulation of photoexcited electrons as pointed out by Z. Hu and C. Y. Jimmy.^{9,23} Thus more photogenerated charge carriers have the chance to participate in the hydrogen generation, leading to an improvement of the photocatalytic activity. Therefore, the incorporation of an optimal amount of transition metal allows increasing both the separation of photogenerated charge carriers and their transfer to surface adsorbed species, enhancing in this way the material photocatalytic activity.

The incorporation of a Co-based metal alloy should also provide the final nano-heterostructures with a magnetic moment which can be used for material purification during its production and for material recovery for recycling and reuse during its active lifetime. Figure 7 displays the magnetic hysteresis loops of CZTS and CZTS-PtCo nanoparticles measured at 5 K. As expected, CZTS-PtCo nano-heterostructures showed a soft ferromagnetic character with a coercive field (H_c) ≈ 65 Oe (Figure 7b). Such hybrid nano-heterostructures, with the ferromagnetic component grown directly onto the

semiconductor, could be also useful for studying nanoscale spin injection into semiconductor nanostructures.^{24, 25}

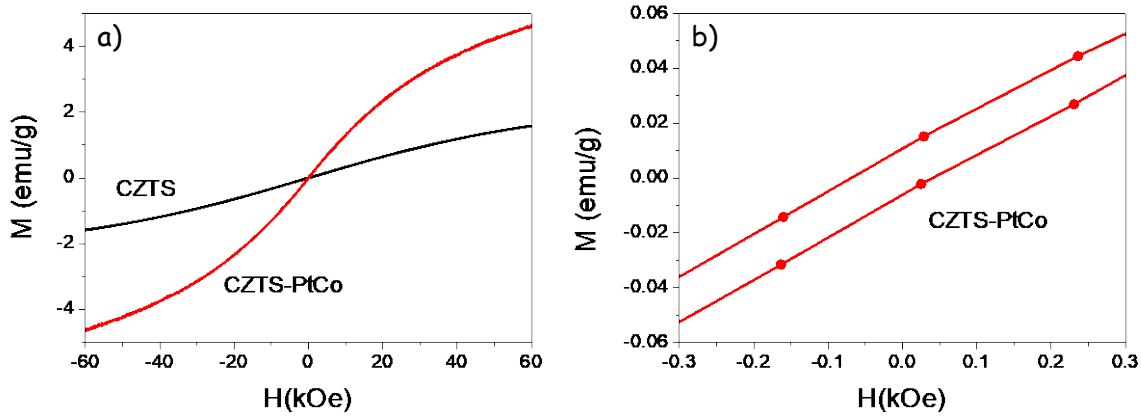


Figure 7. (a) Magnetization vs applied field hysteresis loops measured at 5K for CZTS and CZTS-PtCo (Co/Pt=1) nanoparticles, (b) enlarged part for CZTS-PtCo nanoparticles.

Conclusion

In summary, monodisperse CZTS nanocrystals were synthesized via a hot-injection method and further used as support to produce CZTS-PtCo and CZTS-PtNi nano-heterostructures. CZTS-PtCo materials showed much higher photocatalytic hydrogen generation activity than CZTS and even CZTS-Pt nanoparticles. The higher activity was ascribed to the enhanced charge carrier separation and transport efficiency. The presence of Co enhanced the accumulation of photoexcited electrons in the alloy and facilitated the charge transfer to the surface adsorbed species. Furthermore, the magnetic properties of the metal alloy PtCo attached to the CZTS nanocrystals were preserved, providing the final CZTS-PtCo catalyst with a magnetic moment potentially useful for material purification and recovery.

ASSOCIATED CONTENT

Supporting Information

XRD pattern of CZTS nanocrystals, EDS analysis of CZTS-metal alloy nanocrystals, XPS spectra of CZTS-PtNi nanocrystals and UV-vis-NIR spectra of CZTS-PtCo materials. This material is available free of charge via the Internet at <http://pubs.acs.org>.

AUTHOR INFORMATION

Corresponding Authors

acabot@irec.cat

zyh@cugb.edu.cn

Notes

The authors declare no competing financial interest.

ACKNOWLEDGMENT

This work was supported by the National Natural Science Foundation of China (Grant 21401212), Fundamental Research Funds for the Central Universities (2652015086), the Framework 7 program under project SCALENANO (FP7-NMP-ENERGY-2011- 284486) and the MICINN project ENE2013-46624-C4-3-R. Authors acknowledge the funding from Generalitat de Catalunya 2014 SGR 1638.

REFERENCES

(1) Mokari, T.; Rothenberg, E.; Popov, I.; Costi, R.; Banin, U., Selective Growth of Metal Tips onto Semiconductor Quantum Rods and Tetrapods. *Science* **2004**, *304*, 1787-1790.

(2) Kim, S. M.; Lee, S. J.; Kim, S. H.; Kwon, S.; Yee, K. J.; Song, H.; Somorjai, G. A.; Park, J. Y., Hot Carrier-Driven Catalytic Reactions on Pt–CdSe–Pt Nanodumbbells and Pt/GaN under Light Irradiation. *Nano Lett.* **2013**, *13*, 1352-1358.

(3) Zhao, Q.; Ji, M.; Qian, H.; Dai, B.; Weng, L.; Gui, J.; Zhang, J.; Ouyang, M.; Zhu, H. Controlling Structural Symmetry of a Hybrid Nanostructure and its Effect on Efficient Photocatalytic Hydrogen Evolution. *Adv. Mater.* **2014**, *26*, 1387–1392.

(4) Amirav, L.; Alivisatos, A. P., Photocatalytic Hydrogen Production with Tunable NanorodHeterostructures. *J. Phys. Chem. Lett.* **2010**, *1*, 1051-1054.

(5) Sau, T. K.; Rogach, A. L., Nonspherical Noble Metal Nanoparticles: Colloid Chemical Synthesis and Morphology Control. *Adv. Mater.* **2010**, *22*, 1781-1804.

(6) Strasser, P.; Koh, S.; Anniyev, T.; Greeley, J.; More, K.; Yu, C.; Liu, Z.; Kaya, S.; Nordlund, D.; Ogasawara, H., Lattice-Strain Control of the Activity in Dealloyed Core–Shell Fuel Cell Catalysts. *Nat. Chem.* **2010**, *2*, 454-460.

(7) Stamenkovic, V.; Mun, B. S.; Mayrhofer, K. J.; Ross, P. N.; Markovic, N. M.; Rossmeisl, J.; Greeley, J.; Nørskov, J. K., Changing the Activity of Electrocatalysts for Oxygen Reduction by Tuning the Surface Electronic Structure. *Angew. Chem. Int. Ed.* **2006**, *118*, 2963-2967.

(8) Huang, S.; He, Q.; Zai, J.; Wang, M.; Li, X.; Li, B.; Qian, X., The Role of Mott–Schottky Heterojunctions in PtCo–Cu₂ZnGeS₄ as Counter Electrodes in Dye-Sensitized Solar Cells. *Chem. Commun.* **2015**, *51*, 8950-8953.

(9) Hu, Z.; Jimmy, C. Y., Pt₃Co-Loaded CdS and TiO₂ for Photocatalytic Hydrogen Evolution from Water. *J. Mater. Chem. A* **2013**, *1*, 12221-12228.

- (10) Wu, X. J.; Huang, X.; Qi, X.; Li, H.; Li, B.; Zhang, H., Copper - Based Ternary and Quaternary Semiconductor Nanoplates: Templated Synthesis, Characterization, and Photoelectrochemical Properties. *Angew. Chem. Int. Ed.* **2014**, *126*, 9075-9079.
- (11) Katagiri, H.; Saitoh, K.; Washio, T.; Shinohara, H.; Kurumadani, T.; Miyajima, S., Development of Thin Film Solar Cell Based on $\text{Cu}_2\text{ZnSnS}_4$ Thin Films. *Sol. Energ Mater. Sol. Cells* **2001**, *65*, 141-148.
- (12) Carrete, A.; Shavel, A.; Fontané, X.; Montserrat, J.; Fan, J.; Ibáñez, M.; Saucedo, E.; Pérez-Rodríguez, A.; Cabot, A., Antimony-Based Ligand Exchange to Promote Crystallization in Spray-Deposited $\text{Cu}_2\text{ZnSnSe}_4$ Solar Cells. *J. Am. Chem. Soc.* **2013**, *135*, 15982-15985.
- (13) Yu, X.; Shavel, A.; An, X.; Luo, Z.; Ibáñez, M.; Cabot, A., $\text{Cu}_2\text{ZnSnS}_4$ -Pt and $\text{Cu}_2\text{ZnSnS}_4$ -Au Heterostructured Nanoparticles for Photocatalytic Water Splitting and Pollutant Degradation. *J. Am. Chem. Soc.* **2014**, *136*, 9236-9239.
- (14) Yu, Y.; Yang, W.; Sun, X.; Zhu, W.; Li, X.-Z.; Sellmyer, D.; Sun, S., Monodisperse MPt (M= Fe, Co, Ni, Cu, Zn) Nanoparticles Prepared from a Facile Oleylamine Reduction of Metal Salts. *Nano Lett.* **2014**, *14*, 2778-2782.
- (15) Hull, R. V.; Li, L.; Xing, Y.; Chusuei, C. C., Pt Nanoparticle Binding on Functionalized Multiwalled Carbon Nanotubes. *Chem. Mater.* **2006**, *18*, 1780-1788.
- (16) Jiang, S.; Ma, Y.; Jian, G.; Tao, H.; Wang, X.; Fan, Y.; Lu, Y.; Hu, Z.; Chen, Y., Facile Construction of Pt-Co/ CN_x Nanotube Electrocatalysts and Their Application to the Oxygen Reduction Reaction. *Adv. Mater.* **2009**, *21*, 4953.

- (17) Duong, H. T.; Rigsby, M. A.; Zhou, W.-P.; Wieckowski, A., Oxygen Reduction Catalysis of the Pt₃Co Alloy in Alkaline and Acidic Media Studied by X-Ray Photoelectron Spectroscopy and Electrochemical Methods. *J. Phys. Chem. C* **2007**, *111*, 13460-13465.
- (18) Zheng, J.N.; He, L.L.; Chen, C.; Wang, A.J.; Ma, K.F.; Feng, J.J., One-Pot Synthesis of Platinum Cobalt Nanoflowers with Enhanced Oxygen Reduction and Methanol Oxidation. *J. Power Sources* **2014**, *268*, 744-751.
- (19) Lang, L.; Shi, Y.; Wang, J.; Wang, F.-B.; Xia, X.-H., Hollow Core–Shell Structured Ni–Sn@C Nanoparticles: A Novel Electrocatalyst for the Hydrogen Evolution Reaction. *ACS Appl. Mater. Interfaces* **2015**, *7*, 9098-9102.
- (20) Gao, P.; Liu, J.; Lee, S.; Zhang, T.; Sun, D. D., High Quality Graphene Oxide–Cds–Pt Nanocomposites for Efficient Photocatalytic Hydrogen Evolution. *J. Mater. Chem.* **2012**, *22*, 2292-2298.
- (21) Liu, J.; Yu, X.; Liu, Q.; Liu, R.; Shang, X.; Zhang, S.; Li, W.; Zheng, W.; Zhang, G.; Cao, H., Surface-Phase Junctions of Branched TiO₂ Nanorod Arrays for Efficient Photoelectrochemical Water Splitting. *Appl. Catal. B: Environ.* **2014**, *158*, 296-300.
- (22) Zhang, H.; Lv, X.; Li, Y.; Wang, Y.; Li, J., P25-Graphene Composite as a High Performance Photocatalyst. *ACS Nano* **2009**, *4*, 380-386.
- (23) Wood, A.; Giersig, M.; Mulvaney, P., Fermi Level Equilibration in Quantum Dot-Metal Nanojunctions. *J. Phys. Chem. B* **2001**, *105*, 8810-8815.
- (24) Yuhas, B. D.; Habas, S. E.; Fakra, S. C.; Mokari, T., Probing Compositional Variation within Hybrid Nanostructures. *ACS Nano* **2009**, *3*, 3369-3376.

(25) Lee, J.S.; Bodnarchuk, M. I.; Shevchenko, E. V.; Talapin, D. V., “Magnet-in-the-Semiconductor” FePt–PbS and FePt–PbSe Nanostructures: Magnetic Properties, Charge Transport, and Magnetoresistance. *J. Am. Chem. Soc.* **2010**, *132*, 6382-6391.

TOC

